

## Achievable spatial resolution of time-resolved transillumination imaging systems which utilize multiply scattered light

J. A. Moon,\* P. R. Battle, M. Bashkansky, R. Mahon, M. D. Duncan, and J. Reintjes  
Code 5640, Laser Physics Branch, U.S. Naval Research Laboratory, Washington, D.C. 20375

(Received 22 May 1995)

We describe theoretically and measure experimentally the best achievable time-dependent point-spread-function of light in the presence of strong turbidity. We employ the rescaled isotropic-scattering solution to the time-dependent radiative transfer equation to examine three mathematically distinct limits of photonic transport: the ballistic, quasidiffuse, and diffuse limits. In all cases we follow the constraint that a minimum fractional number of launched photons must be received before the time-integrating detector is turned off. We show how the achievable ballistic resolution maps into the diffusion-limited achievable resolution, and verify this behavior experimentally by using a coherently amplified Raman polarization gate imaging system. We are able to quantitatively fit the measured best achievable resolution by empirically rescaling the scattering length in the model.

PACS number(s): 42.68.Ay, 42.68.Sq, 42.30.-d, 41.85.Ja

### I. INTRODUCTION

Although time-resolved laser-pulse transmission and imaging through both turbid ocean water [1–5] and aerosols [6,7] have been researched extensively, these subjects have undergone a revival recently due to their potential use in nonionizing medical imaging diagnostics [8–22]. Imaging in the presence of turbidity is made difficult because light used to image an object may be scattered between source and detector, which degrades spatial resolution. Time-resolved transillumination imaging works on the principle that at times shortly after the time it takes for light to traverse a turbid material, only those rays which have been forward scattered (and thus not greatly time delayed) will be present in the detector. These rays will obviously have better image information than those that have taken longer random paths to the detector.

Despite the relative intuitive ease in understanding time-resolved imaging, it is not a simple matter to predict the achievable optical resolution of a time-resolved imaging system given a signal-to-noise criterion of at least one photon per pixel arriving in a given time slice. Multiply scattered photons in general obey a time-dependent transport process; theoretical solutions to even the effective-medium time-dependent transport equation are notoriously difficult [23–25]. Nevertheless, we describe in this paper solutions to the radiative transfer problem which effectively describe the achievable spatial resolution of time-resolved imaging through turbid materials.

Before we proceed with a discussion of the theory of photonic transport, it is necessary to define conventions

used in this paper. First, throughout most of this paper we will be discussing the point-spread-function (PSF) of an imaging system which maps spatially and temporally localized point source at the input surface of a turbid slab of thickness  $d$  to the output surface (an analysis is presented below which extends our results to embedded objects). Figure 1 shows the general geometry with the coordinates used in this paper. In reconstructing an image of the broadened point source with a lens, the object plane must be specified. If the direction of propagation  $\hat{\Omega}$  is not randomized, the correct object plane corresponds to the input surface. We refer to this case as OP imaging. (OP stands for object plane, because it corresponds to the object plane without a turbid slab.) If the angles  $\hat{\Omega}$  become randomized, the correct object plane corresponds to the output plane at  $z=d$ . The point source in this case will be broadened to some width on the exit surface and be composed of incoherent point radiators. We refer to this case as EP (exit plane) imaging.

Second, we need to define what we mean by resolution.

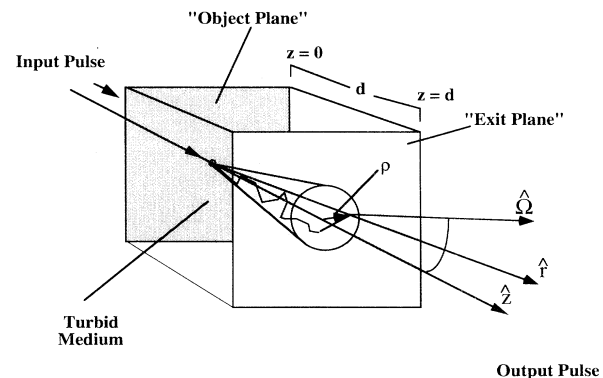


FIG. 1. Configuration used in transillumination imaging with scattered light.

\*Present address: Code 5603, Infrared Materials and Chemical Sensors Section, Naval Research Laboratory, Washington, D.C. 20375.

In incoherent Fourier optics, image quality is governed by a PSF which can be convolved with an intensity in the object plane to obtain the final output image. The PSF will thus broaden a point source at the input of an imaging system to some characteristic width which depends on the imaging system's parameters. The full width at half maximum (FWHM) of the PSF, which we denote as  $\mathcal{R}$ , is a measure of the approximate minimum distance between two point sources at the input of the imaging system that can be "resolved." We define the contrast between two point sources symmetrically placed about  $\rho=0$  as

$$C = \frac{I(\rho_{\max}) - I(0)}{I(\rho_{\max})}, \quad (1)$$

where  $I(\rho_{\max})$  is the intensity at its maximum value, and  $I(0)$  is the intensity at  $\rho=0$ . A FWHM separation of two Gaussian PSF's results in a contrast  $C=7.2\%$ , which we define as our resolution condition. We will also find it convenient to use the half-width  $1/e$  point of the PSF, denoted as  $\mathcal{R}_e$ . The two are related for a Gaussian PSF as  $\mathcal{R}=2\sqrt{\ln(2)}\mathcal{R}_e$ .

The remainder of the paper is outlined as follows. First, we describe the necessary theoretical approaches which allow us to predict imaging performance quantitatively. Second, we discuss imaging experiments performed using a subpicosecond resolution coherently amplified Raman polarization (CARP) gate system which has allowed us to map out the best achievable point-spread-function for our given system sensitivity. Finally, the results are discussed from the viewpoint of applying these techniques to tissue transillumination imaging. Appendixes A and B give details of the theoretical calculations.

## II. THEORY

Although theoretical descriptions of the time-dependent PSF of photons which have traversed a turbid material exist in the published literature [2–5,7,9,17,20], these works have described the optical resolution independent of constraints on system sensitivity. Since real imaging systems have some finite number of photons available to launch, a natural question to ask is what is the best resolution obtainable given some fixed system sensitivity? It is essential that the question of optical resolution be formulated in this manner, as it will be demonstrated below that most theories predict that arbitrarily good resolution can be obtained for arbitrarily short integration times. At these arbitrarily short times, however, the transmitted fraction of photons is so small that no signal arising from any reasonable number of input photons can be measured.

In order to predict accurately the number of photons which will be received in a detector as a function of time, it is necessary to use radiative transport theory. This theory ignores the phase of the photon field, which should be a good approximation for turbid materials composed of small scatterers separated by many optical wavelengths. The radiative transfer equation (neglecting

absorption) for the photon density  $\psi(\mathbf{r}, t; \hat{\Omega})$  (units of  $\text{cm}^{-3}\text{sr}^{-1}$ ) at a space-time point  $(\mathbf{r}, t)$  traveling in a direction  $\hat{\Omega}$  due to a unit point source initially at the origin is [24,25]

$$\begin{aligned} & [c\hat{\Omega}\cdot\nabla + \partial_t + c\mu_s]\psi(\mathbf{r}, t; \hat{\Omega}) \\ & = c\mu_s \int_{4\pi} d\hat{\Omega}' S(\hat{\Omega}, \hat{\Omega}') \psi(\mathbf{r}, t; \hat{\Omega}') + \delta(\mathbf{r})\delta(t)\delta(\hat{\mathbf{r}} - \hat{\Omega}) \end{aligned} \quad (2)$$

where  $\mu_s$  is the scattering coefficient in units of inverse length,  $S(\hat{\Omega}, \hat{\Omega}')$  is the probability density that a photon traveling in the direction  $\hat{\Omega}'$  will scatter into a direction  $\hat{\Omega}$ , and  $c$  is the effective speed of light in the material. The scattering length  $l_s$ , i.e., the average distance between collisions, is  $l_s = \mu_s^{-1}$ .

There are three physically distinct limits of time-dependent photon transport. Light obeying the first limit, the ballistic limit, corresponds to those photons which have traversed the sample without scattering. The third limit, the diffusion limit, contains those photons that have scattered enough between source and detector so that they have essentially lost all their directional information.

In between these two limits, there may be photons which have scattered in the materials, but not sufficiently to obey diffusion statistics. Historically, this regime has been known by many names. Bucher and co-workers [6] called this regime the "forward scatter" regime, while in the more extensive theoretical and experimental work of Mooradian *et al.* [7], these photons were named "type-II" photons ("type I" and "type III" corresponding to the ballistic and diffuse limits, respectively). In the Soviet literature [5], photons in this regime are usually labeled by the variously applicable mathematical approximations to the radiative transfer equation which best describe them [e.g., small-angle approximation (SAA) and small-angle diffusion approximation (SADA) [5]]. Lately, photons in this regime have been associated with the term "snake light," although more than one definition of this term appears in the literature [13–16]. We will use the term "quasidiffuse" to label photons in this regime in the present work, because we will show below that these photons will generally display optical resolutions closer to the diffusion limit than the ballistic limit when the ballistic component is immeasurably small.

### A. Ballistic limit

The photons which arrive at the causal time without scattering in the turbid material are called "ballistic" photons,  $\psi_b$ . They are described by the ballistic or "streaming transport" propagator, i.e., the response of the system ignoring the photons scattered back into the direction of propagation. This quantity is obtained by solving Eq. (2) with the scattering function  $S$  set to zero. The result is

$$\psi_b = K(\mathbf{r}, t; \hat{\Omega}) = \frac{c\mu_s}{4\pi} e^{-\mu_s r} \frac{\delta(r - ct)}{r^2} \delta(\hat{\mathbf{r}} - \hat{\Omega}). \quad (3)$$

Two things are immediately observed about ballistic

photons from Eq. (3). First, they retain perfect directional information, and thus are encoded with the diffraction-limited resolution of the optical imaging system (and so OP imaging should be used). Second, their intensity drops exponentially with the number of scattering lengths. Thus, even assuming  $10^{19}$  input photons (around one  $J$ ) in  $10^4$  pixels, the quantum limit (i.e., one photon per pixel) is reached in about 35 scattering lengths. Ballistic photons have been observed for attenuations [21] up to  $e^{33}$ . Imaging through turbid materials thicker than this will require use of photons which have scattered at least once in the material.

### B. Diffusion limit

The ‘‘opposite’’ limit of transport theory, the diffusion limit, occurs when the photons traversing the material have scattered so much that they have lost almost completely their initial directional information. In this limit, the radiative photon density is approximated by

$$\psi(\mathbf{r}, t; \hat{\Omega}) \simeq \frac{1}{4\pi} n(\mathbf{r}, t) + \frac{3}{4\pi c} \mathbf{J} \cdot \hat{\Omega}, \quad (4)$$

where

$$n(\mathbf{r}, t) = \int_{4\pi} d\hat{\Omega}' \psi(\mathbf{r}, t; \hat{\Omega}') \quad (5)$$

and

$$\mathbf{J}(\mathbf{r}, t) = c \int_{4\pi} d\hat{\Omega}' \psi(\mathbf{r}, t; \hat{\Omega}') (\hat{\Omega}'). \quad (6)$$

Inserting Eq. (4) into Eq. (2) yields the equation of continuity and Fick’s law with a time-varying flux, respectively, i.e.,

$$\nabla \cdot \mathbf{J} + \partial_t n = \delta(t) \delta(\mathbf{r}) \quad (7)$$

and

$$D \nabla n + \frac{1}{c(1-g)\mu_s} \partial_t \mathbf{J} + \mathbf{J} = \mathbf{0}, \quad (8)$$

where  $D = c/[3(1-g)\mu_s]$ . The anisotropy factor  $g$  is defined by

$$g = \int_{4\pi} d\hat{\Omega}' S(\hat{\Omega} \cdot \hat{\Omega}') \hat{\Omega} \cdot \hat{\Omega}', \quad (9)$$

where we have assumed for simplicity that  $S$  is a function of only the angle between its two arguments.

The diffusion equation is obtained by substituting Eq. (7) into Eq. (8). The result is

$$[-D \nabla^2 + \partial_t] n(\mathbf{r}, t) = \delta(t) \delta(\mathbf{r}), \quad (10)$$

where we have also neglected the term proportional to  $\partial_t \mathbf{J}$  in Eq. (8).

From the above definitions we can also define a transport length  $l_t = f_d(g) l_s$ , where  $f_d(g) = 1/(1-g)$ . This length represents the distance over which the direction  $\hat{\Omega}$  becomes completely randomized.

Equation (10) has a well-known Green’s function solution for a slab [26] where the boundary condition is taken to be  $n(\rho, z=0, t) = n(\rho, z=d, t) = 0$ ,

$$n(\mathbf{r}-\mathbf{r}', t-t') = \sum_{m=-\infty}^{\infty} G(\rho-\rho', z-z'+2md, t-t') - G(\rho-\rho, z+z'+2md, t-t'), \quad (11)$$

where  $G(r, t)$  is the infinite-space propagator

$$G(r, t) = \frac{e^{-r^2/4Dt}}{(4\pi Dt)^{3/2}} \quad (12)$$

and  $r = \sqrt{z^2 + \rho^2}$ .

Letting  $n=0$  on the physical boundaries is only an approximation of the boundary conditions. A better approximation is to express the boundary conditions to Eq. (2) in terms of  $n$  and  $\mathbf{J}$ . The resulting boundary conditions are approximately equivalent to stating that the number density goes to zero on the extrapolated surfaces [27] at  $z = -\frac{2}{3}l_t$  and  $z = d + \frac{2}{3}l_t$ . We may thus use the Green’s function for  $n(\rho, z, t) = 0$  on the boundaries, provided we use the correct surfaces.

In order to calculate the total flux calculated from Fick’s law received in a detector on the output surface of the slab, we take the following actions. First, for slabs that are many transport lengths thick, the effective size of the point source, which is about one  $l_t^3$ , will be much smaller than the output resolution. Thus we may replace the source with a  $\delta$  function embedded in the slab at one transport length deep. Second, we will use a square window integrating gate on the detector, and ignore the causal transit time for the moment (this approximation is discussed fully below). Third, we will integrate over the detector’s area  $A = \pi a^2$ . There are two detector size limits which interest us: the case  $a \gg d$  and the case  $a \ll d$ . We usually encounter the second situation in experiments where the size of the pixel at the center of the PSF (the maximum fractional number of photons will be received in this pixel) is much smaller than the PSF and the thickness of the sample.

Thus, for the total fractional number of photons  $N$  collected at some short time  $\tau$  for a detector at  $d$ , we obtain

$$N = D \nabla_z \int_0^\tau dt \int_A \rho d\rho d\theta n(\rho, z, t)|_{z=d}. \quad (13)$$

Equation (13) is solved below for a given received photon fraction  $N$ , which sets the necessary integration time  $\tau$ . To solve for the PSF, we remember from Eq. (4) that the directional information  $\hat{\Omega}$  in the diffusion limit is by definition lost, so for the PSF system we must use the intensity profile on the slab output surface (i.e., EP imaging). The PSF in the diffusion case is given by the  $\rho$  dependence of Eq. (11) evaluated at the integration time  $\tau$  and  $z=d$ . Examination of Eqs. (11) and (12) shows that the  $\rho$  dependence is approximately Gaussian with a  $1/e$  half-width  $\mathcal{R}_e$

$$\mathcal{R}_e = \sqrt{4D\tau}. \quad (14)$$

The ratio  $\mathcal{R}_e/d$  is a recurring quantity in Eq. (13). We therefore define a quantity  $x_0$  by

$$\mathcal{R}_e = d/x_0 \quad (15)$$

and substitute it into Eq. (13). By expanding Eq. (13) at

short times, we find that only the  $m=0$  and  $-1$  terms contribute significantly, and we obtain the result that the resolution at a particular fractional number of received photons  $N$  scales as Eq. (15), where the quantity  $x_0$  is given by the solution to the transcendental equation

$$e^{-x_0^2} = \alpha N x_0, \quad (16)$$

where  $\alpha = (\sqrt{\pi d}) / (2l_t)$ . When  $\alpha N$  goes between  $10^{-10}$  and  $10^{-20}$ ,  $x_0$  only changes between 4.7 and 6.8, respectively. Thus the achievable resolution is an extremely weak function of all parameters except sample thickness.

This is a somewhat surprising result, but has a simple physical explanation. The received power is predicted to rise extremely quickly in the diffusion limit, but the resolution is only a weak function (the square root) of the integration time. Thus one merely needs to open the time gate slightly to make a large difference in the received intensity at short times, which will not affect the width of the PSF significantly.

The optimal time gate  $\tau$  required to obtain the best achievable spatial resolution in the diffusion limit is

$$\tau = \frac{\mathcal{R}_e^2}{4D} \simeq \frac{3d^2}{4x_0^2 c l_t}. \quad (17)$$

Equation (17) predicts that short integration times will be necessary for thin samples. Since the diffusion approximation does not obey causality, it will break down at short times. We therefore need to specify what minimum thickness can be used in this limit. Intuitively, one might expect that as the necessary time gate becomes large compared to the causal transit time, the diffusion equation should describe the measured signal to arbitrary precision. We show in Appendix A by calculating the first transport correction to diffusion theory that, provided the time gate satisfies  $c\tau/l_t \gg (d/l_t)^{2/3}$ , diffusion theory should describe the measured signal.

Defining the causal transit times as  $\tau_c = d/c$ , we thus find that the diffusion approximation is valid for

$$\frac{\tau}{\tau_c} = \frac{3d}{4x_0^2 l_t} \gg \left( \frac{l_t}{d} \right)^{1/3}. \quad (18)$$

Taking  $x_0 \simeq 5$ , we find that the inequality of Eq. (18) is satisfied for samples greater than 14 transport lengths thick. We find below that for samples much thicker than this limit the diffusion approximation adequately describes the measured signal at all times.

The restriction that the integration time must be much larger than the causal time can be removed to first approximation by utilizing random walk theory. Gandjbakhche, Nossal, and Bonner [17] have shown that the central-limit propagator (i.e., a Gaussian propagator) can be substituted into a random walk on a cubic lattice to obtain more accurate modeling of transport where the diffusion equation solution is not as good an approximation. Examination of the method, however, shows that it ultimately relies on substitution of a causally corrected propagator in the Green's function propagator identical to  $G(r, t)$  used above except with  $t \rightarrow t - \tau_c$ . We compare

the optimal resolution obtained by numerically integrating the causally corrected and uncorrected (acausal) Green's functions (with  $N=10^{-15}$ ), along with the asymptotic limit  $\mathcal{R}_e = d/x_0$  in Fig. 2. Even with this stringent condition on the number of received photons, there is little difference in the three methods for samples greater than about 45 transport lengths thick.

The turbid slab with zero density on the extrapolated surfaces is the most physically appealing solution in the diffusion limit. Many other permutations of boundary conditions are possible in this limit. For instance, it is possible to ignore completely that any boundaries are present and use the infinite space Green's function  $G(r, t)$  for the propagator. In the absence of boundaries, one may also use either the integrated photon density or flux to model the received signal. The results of the various permutations of boundary conditions and integrated quantities (i.e., either flux or density) are summarized in Table I for the case when the detector radius  $a \gg d$ . In all cases, a transcendental equation for  $x_0(\alpha N, p)$  of the form

$$\alpha N x_0^p = e^{-x_0^2} \quad (19)$$

is obtained, where  $p=1$  or  $3$ , and  $\alpha$  is some combination of parameters which typically vary by less than a few orders of magnitude ( $\alpha N$  will always be very small in any case). The cases where  $a \ll d$  can be obtained from the information in Table I by letting  $\alpha \rightarrow (d/a)^2 \alpha$  and  $p \rightarrow p-2$ . Figure 3 plots  $x_0$  versus  $\alpha N$  for the three relevant  $p$  values. The quantity  $x_0$  scales extremely slowly with  $\alpha N$  in each case, and varies little in value relative to the various approximations used. We conclude that the resolution scaling law is robust to any reasonable combination of boundary conditions and detector configurations.

For embedded objects, one may calculate the flux through any small volume of the sample by constructing a source term from the input point source to some point in the sample  $(\rho, z, t')$ , propagating it to the exit surface in a total time  $\tau$ , and averaging over  $t'$ . This procedure was explicitly calculated in a slab geometry in Ref. [17] for the random-walk theory; the continuous space analog can

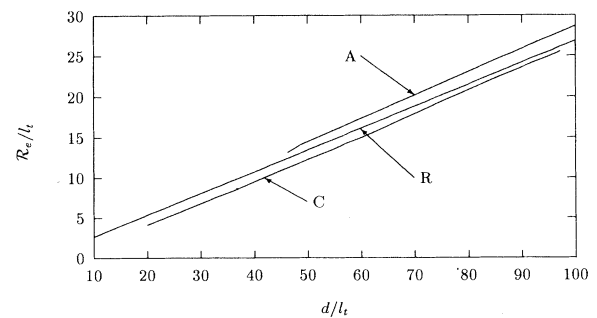


FIG. 2. Optimal resolution in the diffusion limit at an attenuation threshold of  $N=10^{-15}$  obtained via three different methods. Curve R: asymptotic solution  $\mathcal{R}_e = d/x_0$ . Curves C and A: numerically integrated causally corrected and uncorrected solutions to the diffusion equation, respectively.

TABLE I. Resolution scaling laws for  $\mathcal{R}_e = d/x_0(\alpha N, p)$ , assuming various geometries and boundary conditions. In all cases except the embedded case, we assume the detector radius  $a \gg d$ . For  $a \ll d$ , let  $\alpha \rightarrow (d/a)^2 \alpha$  and  $p \rightarrow p-2$ . The resolution scaling law for the “embedded at  $z=\delta$ ” case is  $\mathcal{R}_e^E(\delta, d) = \sqrt{\delta(d-\delta)}/x_0$ .

Geometry	Integrated quantity	$\alpha$	$p$
Infinite	Density	$\frac{4\sqrt{\pi}l_t}{3d}$	3
Slab	Density	$\frac{\sqrt{\pi}d}{18l_t}$	3
Infinite	Flux	$\frac{2\sqrt{\pi}d}{2l_t}$	1
Slab	Flux	$\frac{\sqrt{\pi}d}{2l_t}$	1
Embedded $z=\delta$	Density	$\frac{1}{\sqrt{\pi}} \left[ \frac{4\pi}{3} \right]^{3/2} \frac{\delta(d-\delta)}{a^2}$	1

be constructed with the Green’s function described above. The calculation is outlined in Appendix B, the result of which is quoted here and summarized in Table I for an object embedded at a depth  $z=\delta$ , where  $0 < \delta < d$ . The resolution scaling law for  $\mathcal{R}_e^E(\delta, d)$ , the embedded resolution, for an object placed between source and detector at  $\delta$  reduces to

$$\mathcal{R}_e^E(\delta, d) = \mathcal{R}_e(d) \frac{\sqrt{\delta(d-\delta)}}{d} = \frac{\sqrt{\delta(d-\delta)}}{x_0}, \quad (20)$$

where the solution for  $x_0$  in this case is also near 5, and  $\mathcal{R}_e(d)$  is the achievable  $1/e$  resolution for a slab of thickness  $d$ . The achievable width of the PSF for the object embedded at  $\delta=d/2$  is exactly twice as narrow as that possible for a slab of thickness  $d$ , as expected from more heuristic arguments presented previously [22].

We have shown above that even in the diffusion limit boundary conditions contribute little at short times, and that the resolution scales in a simple fashion for small embedded objects. Since the diffusion limit of radiative

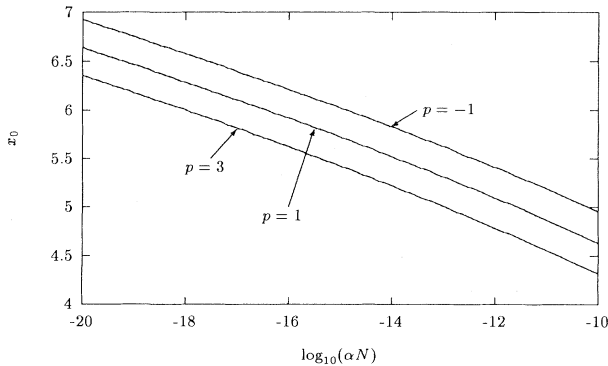


FIG. 3. Solution to the transcendental equation governing the diffusion resolution scaling law  $\mathcal{R}_e = d/x_0$  for all permutations of geometries and boundary conditions.

transfer is most sensitive to these conditions, we can thus be confident that applying solutions to the radiative transfer equation for infinite geometries when the diffusion limit is invalid will yield reasonably correct answers for the predicted best achievable resolution.

### C. Quasidiffuse limit

The ballistic and diffusion limits are the simplest solutions to the radiative transfer problem. However, these solutions by no means represent a complete physical picture of radiative transfer in all circumstances. In order to fully describe the imaging problem, the quantity  $\psi(\mathbf{r}, t; \hat{\Omega})$  must be calculated for the cases when it is not a virtually isotropic function of  $\hat{\Omega}$  and the ballistic component is immeasurably small.

Unfortunately, direct analytic solution of Eq. (2) has not proved possible to date for an arbitrary scattering function  $S$ . In this paper, we solve Eq. (2) when  $S=1/(4\pi)$  (isotropic scattering). We then argue that when  $g > 0$ , the scattering length  $l_s$  in this solution can be rescaled to some length  $l_r = f(g)l_s$ , where  $f(g)$  is assumed to depend only on  $g$ . That this rescaling should be reasonably justified can be seen from solutions to the small-angle approximation (SAA) of the radiative transfer equation [3]. These solutions describe a photon’s behavior in a strongly forward-peaked scattering material ( $g \simeq 1$ ) close to the source. The amplitude decays in this solution as  $(1-g)\mu_s d$ , not  $\mu_s d$  as in Eq. (3). Unlike Eq. (3), however, the angular portion is no longer a  $\delta$  function, so that rescaling  $l_s$  by replacing  $l_s \rightarrow f_d(g)l_s$ , where  $f_d(g) = 1/(1-g)$  (the diffusion-limited length rescaling) in Eq. (3) should overpredict the achievable resolution. Physically, this best-case rescaling would replace the many collisions it takes in a large- $g$  material to randomize  $\hat{\Omega}$  with a single, isotropically distributed collision event occurring over an average distance  $l_t$ . In Sec. III, we will find that this best-case scenario in fact does overpredict the achievable resolution.

We now calculate solutions to the isotropic-scattering radiative transport problem useful at short times. In a previous publication [28] we outlined a solution to this problem using a Markov chain approach. In this approach, one asks the following question: Given that the probability  $P^{(n)}(\mathbf{r}', t'; \hat{\Omega}')$  of arriving at a given space-time point  $(\mathbf{r}', t')$  traveling in a given direction  $\hat{\Omega}'$  after experiencing  $n$  collisions is known, what is the probability  $P^{(n+1)}(\mathbf{r}, t; \hat{\Omega})$  of arriving at a space-time point  $(\mathbf{r}, t)$  traveling in a direction  $\hat{\Omega}$  after the collision at  $(\mathbf{r}', t', \hat{\Omega}')$ ? The relationship between the  $n$ th and the  $n$ th plus first collision is

$$P^{(n+1)}(\mathbf{r}, t; \hat{\Omega}) = \int d^3\mathbf{r}' dt' d\hat{\Omega}' K(\mathbf{r}-\mathbf{r}', t-t'; \hat{\mathbf{R}}-\hat{\Omega}') \times P^{(n)}(\mathbf{r}', t'; \hat{\Omega}'), \quad (21)$$

where  $\hat{\mathbf{R}}$  is the unit direction vector along  $\mathbf{r}-\mathbf{r}'$ . The function  $K$  is precisely the ballistic or streaming transport propagator given by Eq. (3). This approach is formally equivalent to solving the radiative transfer equation, as is proven in Ref. [24]. In fact, one can show that

$$c\mu_s\psi(\mathbf{r},t;\hat{\Omega}) = \sum_{n=1}^{\infty} P^{(n)}(\mathbf{r},t;\hat{\Omega}). \quad (22)$$

Note that the  $n=1$  term corresponds to the ballistic solution, i.e., Eq. (3). This series is also known as a ‘‘collision expansion’’ in the transport literature [24].

The asymptotic solution to Eq. (21) was quoted in Ref. [28], and we give the explicit details in Appendix A. The quantities which concern us are the  $l=0$  and 1 terms of the expansion of  $P^{(n)}$  in the spherical harmonics of argument  $\hat{\Omega}$ . These functions are shown in Appendix A to correspond to  $\mathcal{J}_0^{(n)}(r,t)$  (the  $l=0$  term), the photon arrival probability integrated over all angles  $\hat{\Omega}$ , and  $C^{(n)}(r,t)$ , the cosine of the angle between  $\hat{\mathbf{r}}$  and  $\hat{\Omega}$  after  $n$  collisions (the  $l=1$  term divided by the  $l=0$  term). These two functions were checked against continuous time and space Monte Carlo simulations in Ref. [28]. In all cases there was found to be excellent agreement between the Monte Carlo and the analytic theory.

To extract the PSF from the above information, we assume that EP imaging should be used (this is justified below). We use a plane detector some distance  $d$  from the point source which integrates in time between the causal time  $d/c$  and a time  $\tau+(d/c)$ . We are interested in the intensity crossing  $d$  at points  $\rho$  perpendicular to  $d$ . Because the intensity  $\mathcal{J}$  depends only on  $r = \sqrt{d^2 + \rho^2}$ , integrated intensities crossing the detector at positions  $\rho$  are the same as those crossing the detector at  $\rho=0$ , but integrated only up to a time  $\tau(\rho) = \sqrt{[(d/c)+\tau]^2 - \rho^2} - (d/c)$ . The EP point-spread-function is therefore

$$F(\rho,d,\tau) = \sum_{n=2}^{\mathcal{N}} F(n,\rho,d,\tau), \quad (23)$$

where

$$F(n,\rho,d,\tau) = \int_{d/c}^{\sqrt{[(d/c)+\tau]^2 - \rho^2}} dt \mathcal{J}_0^{(n)}(\sqrt{\rho^2 + d^2}, t), \quad (24)$$

where we have truncated the asymptotic series at some collision number  $\mathcal{N}$ . We find that  $\mathcal{N}=30$  is sufficient to ensure convergence without exceeding the range of validity for the expansion for thicknesses  $d < 30\text{--}35$  scattering lengths.

We are interested in the achievable PSF, which we calculate by requiring an integration time  $\tau$  such that the total number of photons crossing the exit surface equals some number. The resulting achievable PSF is plotted in Fig. 4 for several  $d$  values using the criterion that one photon in  $10^{15}$  ( $N = 10^{-15}$ ) is collected. We plot the contribution to the PSF by each collision number for the same set of thicknesses in Fig. 5. In Fig. 6, we plot the FWHM of the PSF as a function of thickness for three different attenuation criteria on the received number of photons, along with the diffusion limit (where we use the FWHM value). Figure 7 shows the time gates used to get the optimal PSF at an attenuation criterion of  $N = 10^{-15}$ . We see that changing the attenuation criterion by ten orders of magnitude has little effect on the achievable resolutions, showing that these limits are extremely robust against variations in collection conditions. We thus expect that practically any time-resolved imaging apparatus

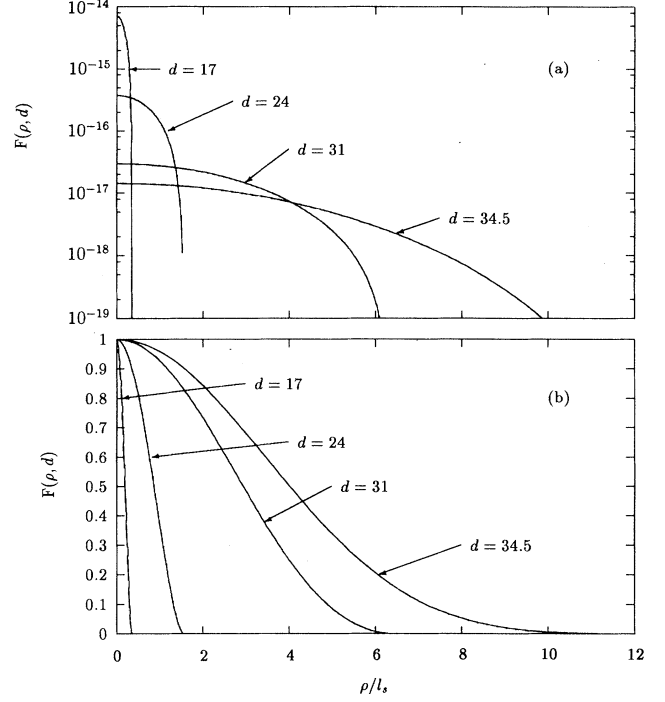


FIG. 4. Optimal point-spread-functions for four different thicknesses and a collection efficiency of one photon in  $10^{15}$  in the quasidiffuse regime.

that can meet the optimum time-gate criterion will yield achievable resolutions close to these limits.

In Ref. [28] it was shown that EP imaging should be used in the quasidiffuse limit. We show in Appendix A that the directional information in this isotropic-scattering solution is dependent only upon the previous collision for any  $n$ , so we expect (and it was observed in Ref. [28]) that  $C^{(2)} \simeq C^{(n)}$  for any  $n$ . Therefore, using  $C^{(2)}$  only, we plot in Fig. 8 the effective average numerical aperture  $N_a \simeq \sqrt{1 - [C^{(2)}(d,\tau)]^2}$  of the rays passing through the surface at  $z=d$  as a function of the time gate. By comparing the times in Fig. 8 to the optimal time gates shown in Fig. 7, we see that the effective numerical aperture of the rays is sufficiently high to sub-

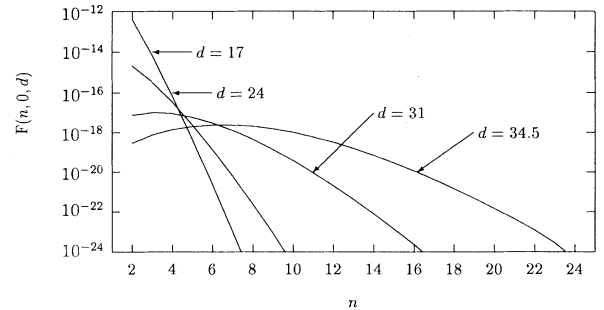


FIG. 5. Contributions from each number of collisions for four different thicknesses and a collection efficiency of one photon in  $10^{15}$  in the quasidiffuse regime.

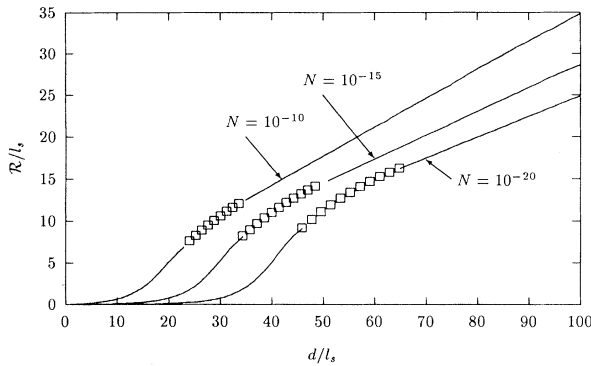


FIG. 6. Best achievable resolution (FWHM of PSF) vs sample thickness for three different collection efficiencies. The curves are calculated from the isotropic-scattering solution to the radiative transfer equation described in the text. The diamonds represent a cubic spline between the diffuse and quasidiffuse limits, where neither approximation works well.

tend the entire lens in an  $f/30$  imaging system (which is used in the experiments below).

### III. EXPERIMENT

At least five experimental conditions are necessary to observe quasidiffuse photons unambiguously. First, the integrating time of the system must be much shorter than the transit time of the photons through the turbid material. This ensures that the photons collected have not deviated significantly from their initial path and still have a “memory” of their initial launch direction. For centimeter-sized samples, this condition requires subpicosecond temporal resolution. Second, the number of scattering lengths  $l_s$  of a material of thickness  $d$  should be large enough so that no ballistic light is present. The simplest way to ensure that the ballistic component is not present is to increase  $d/l_s$  of the sample while monitoring the ballistic signal. Since the ballistic signal drops exponentially with  $d/l_s$ , a clear threshold is observable. It is not absolutely necessary that this condition is satisfied

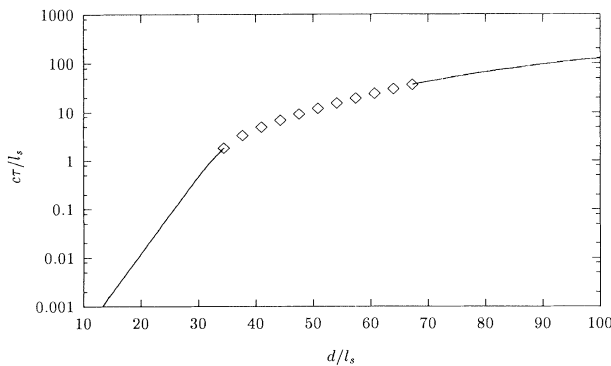


FIG. 7. Optimal time gate needed for collecting one photon in  $10^{15}$  launched. The diamonds represent a cubic spline between the quasidiffuse and diffuse limits.

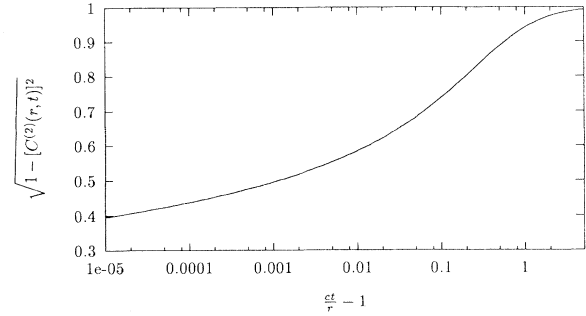


FIG. 8. Effective numerical aperture of the rays emitted from the exit surface as a function of time.

to see quasidiffuse light; however, it is easy to mistake the ballistic component for a quasidiffuse component unless the ballistic component is completely eliminated. For a system with which can collect one photon in  $10^{10}$  launched per pixel, this condition requires samples in excess of 23 scattering lengths thick. Third, the system must have a large enough field of view so that an area comparable to the square of the sample thickness can be observed (since the width of the diffusion limited point-spread-function is a significant fraction of the sample thickness). Finally, the system’s effective  $f/\#$  must be small enough so that a significant portion of scattered light will be collected by the imaging optics; otherwise, the collection optics will act as a spatial filter and discard signal amplitude.

Even if all these conditions are met, it may be the case that only photons which obey diffusion statistics are measurable if the sample thickness (measured in numbers of transport lengths) is sufficiently large. In the best-case scenario described above, the theory is scaled directly into the anisotropic case by replacing  $l_s$  with  $l_t$ . By observing where the diffusion limit is approached (Fig. 6), we estimate that samples shorter than about 30 transport lengths are needed if there is to be any hope of observing quasidiffuse photons. This is the fifth condition.

These conditions were met by the imaging system pictured schematically in Fig. 9. The system is based on the coherently amplified Raman polarization (CARP) image gate described elsewhere [29]. A frequency-doubled

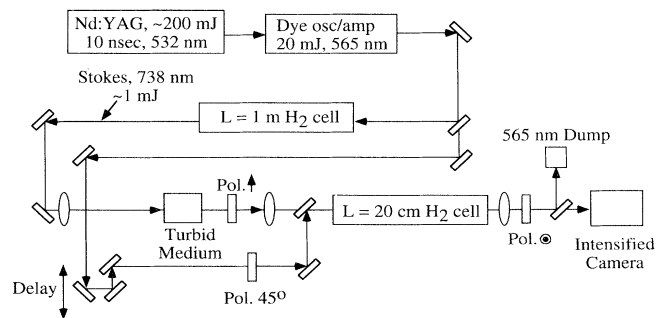


FIG. 9. Schematic of experiments performed using the coherently amplified Raman polarization (CARP) gate.

Nd:YAG (yttrium aluminum garnet) oscillator/amplifier operating at a 10-Hz repetition rate is used to pump a broadband ( $\sim 160 \text{ cm}^{-1}$ ) dye laser/amplifier which produces 20 mJ per pulse centered at 565 nm (not shown). The 565-nm pulses are split into two paths. One path goes to a 1-m-long cell containing 300 psi of molecular hydrogen. The output of this cell contains approximately 1 mJ of Stokes-shifted light centered at 738 nm, which after spatial filtering is used to illuminate the sample as a 0.62-mm full width at half maximum (FWHM) Gaussian beam. The second part of the 565-nm beam, after passing through an adjustable optical delay, is used to pump a 20-cm-long hydrogen cell amplifier (at the same pressure as the 1-m generating cell) after the sample. The polarization of the pump beam is at a  $45^\circ$  angle to the polarization of the Stokes used to illuminate the sample. After a final polarizer orthogonal to the illuminating Stokes polarization, the light emerging from the output face of the cell was imaged onto an intensified camera. Images of  $200 \times 200$  pixels were digitized and stored on a computer after averaging over 200 laser shots.

In this particular configuration, the temporal resolution of the imaging system was 250-fs FWHM, the field of view was  $\sim 1$  cm, and the spatial resolution (set by the system Fresnel number) was comparable to the width of the illuminating beam. We take the measured illuminating beam width of 0.62-mm FWHM to be the ballistic resolution of the system. We measured (using calibrated neutral density filters) that the system could measure a sample attenuation of about  $10^{10}$  at a signal-to-noise ratio of unity in a single shot.

A series of custom-made optical cells with  $x$  and  $y$  dimensions (perpendicular to the illumination axis) of  $1 \times 1$  cm and having path lengths ranging between 2 mm and 2 cm were used in these experiments. The solution in the cells consisted of dielectric spheres in water or in glycerol with the concentration chosen to have a scattering length of  $l_s \approx 0.25$  mm in all cases. We varied the anisotropy parameter  $g$  by changing the type of scatterers: for  $g = 0.66$  we used a Ropaque-62 solution; for  $g = 0.78$  we used an Intralipid solution; for  $g = 0.86$  and  $0.92$  we used 3- and  $1.6\text{-}\mu\text{m}$ -diameter polystyrene spheres, respectively; and for  $g = 0.995$  we used  $11\text{-}\mu\text{m}$ -diameter glass beads suspended in glycerol.

Figure 10 shows the images of the received PSF taken through the  $g = 0.92$  solution 25 scattering lengths thick ( $d = 1$  cm) at various gating times. At this density the ballistic component is unobservable with this system. Ultimately, we increased the concentration to make this 1-cm-long sample a total of 40 scattering lengths thick in the best achievable PSF measurements below.

We measured the best achievable resolution with this system by adjusting the delay of the time gate until the minimum point-spread-function was observed at a signal-to-noise ratio of about unity. The signal was then averaged for 200 shots to bring the signal up to a usable level. We plot the results of these measurements, the best-achievable FWHM of the PSF as a function of  $d/l_s$ , for the two largest  $g$  values, in Fig. 11. For sufficiently short samples the ballistic resolution is obtained (indicated in Fig. 11 by the labeled horizontal line). Eventually,

the ballistic component disappears. The time-gate position is then delayed relative to the now-invisible ballistic component until a signal appears, and the next point is taken. The solid line fits to these data are discussed further below.

For these particular imaging optics, no component of light was clearly visible after the ballistic component disappeared for  $g$  values less than 0.86. These  $g$  values correspond to the Intralipid and Ropaque-62 solutions.

The images obtained through the glass-bead and glycerol solution ( $g = 0.995$ ) showed an interesting property. Figure 12 shows a series of images taken through "69" scattering lengths total. We use quotation marks to emphasize that in this case the scattering length is probably not a valid physical quantity. At the concentrations of glass spheres that we used, the interbead separation was on the order of the sphere diameter. We therefore expect that several scattering events add coherently, which is not described by the radiative transfer theory. Further evidence that this is the case can be observed in the images of Fig. 12, which shows a speckle size significantly

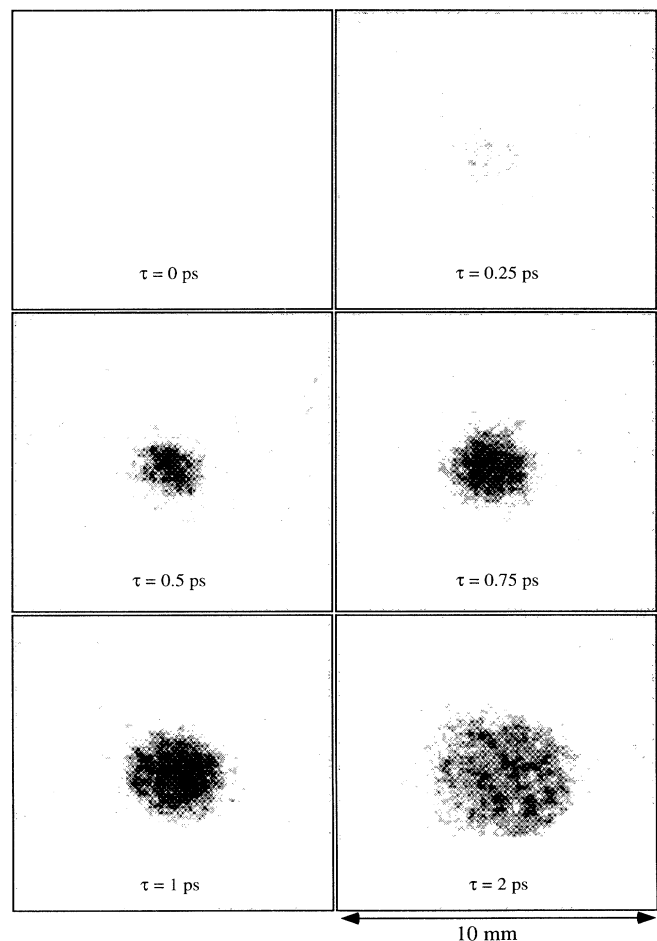


FIG. 10. Series of images taken through 25 scattering lengths of polystyrene spheres suspended in water ( $g = 0.92$ ) when the ballistic component is not present. The physical sample thickness is 1 cm.

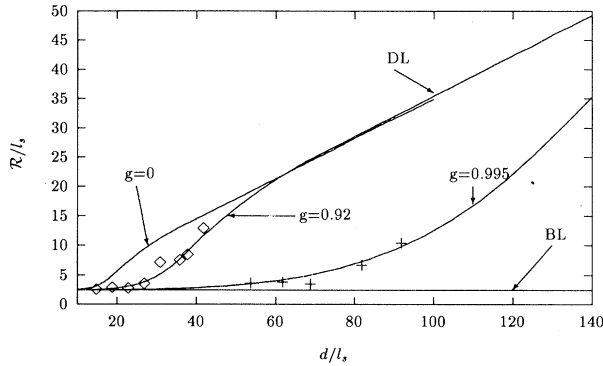


FIG. 11. Experimentally obtained best achievable resolution (FWHM of PSF) for labeled  $g$  values. The solid curves are fits from the model described in the text. The scattering length was  $l_s \approx 0.25$  mm for all points.

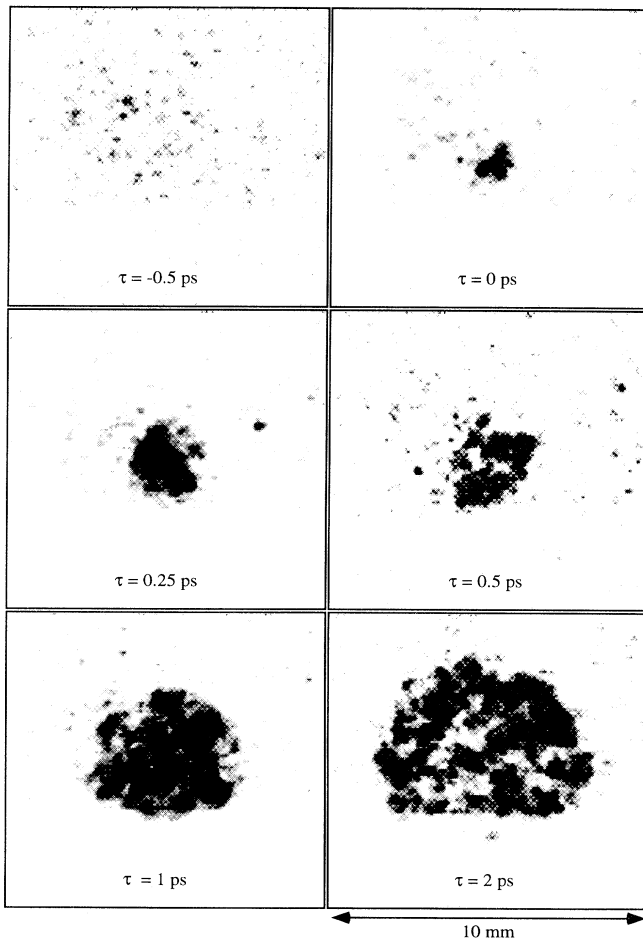


FIG. 12. Series of images taken through  $\mu_s d = 69$  scattering lengths of  $g = 0.995$  glass spheres in glycerol. The speckle size is much larger than expected for an incoherent of the same size, showing that the scattering is correlated. The physical sample thickness is 1 cm.

larger than expected for a PSF of this diameter composed of incoherent point radiators.

#### IV. DISCUSSION

Rescaling the isotropic-scattering solution to the radiative transport equation with the diffusion-theory transport length  $l_t$  gives a very poor fit to the data in Fig. 11. As a first approximation we did fit our best achievable PSF data with the solution to the above rescaled isotropic transport problem. In the theory we integrated the solution from the causal time to a time  $\tau_g$ , rather than over a certain pulse width. This should not affect the results as there are no measurable photons in the signal before a pulse width. We rescaled the scattering length to a reduced scattering length  $l_r = f(g)l_s$ , where  $f(g)$  is some unknown function of  $g$ . We find that  $f(0.92) \approx 2$  and  $f(0.995) \approx 7.5$  give an adequate fit to the data.

We have thus demonstrated that rescaling the isotropic-scattering solution to the transport equation to fit the experimental data yields a scaling function which is *significantly* smaller than the standard  $f_d(g) = 1/(1-g)$  scaling predicted from the diffusion limit. Apparently the diffusion-limited resolution is reached far more quickly than the standard scaling would predict. By extrapolating the fit in Fig. 11 for the case of  $g = 0.92$ , the diffusion-limited resolution is reached in about 60 scattering lengths, or about five transport lengths. This is not completely unreasonable, although it is still a remarkably short thickness. In the case of  $g = 0.995$ , however, the extrapolated theoretical diffusion-limited resolution is reached in about 225 scattering lengths, or about  $l_t \sim 1$ . This comparison is of dubious value, however, because the radiative transport theory does not well describe the close-packed nature of the sample. Clearly more work can be done in this area.

The above-measured resolutions are measurements of the width of the output PSF  $\mathcal{R}(d)$  for a slab of thickness  $d$ , and not measurements of achievable resolution of embedded objects. Recall that, in the diffusion limit, we showed above that the width of the achievable PSF  $\mathcal{R}_e(\delta, d)$  for an object embedded at  $\delta$  in a slab of thickness  $d$  scales as the geometric average of the achievable resolutions for slabs of thickness  $\delta$  and  $d - \delta$ , respectively. This suggests that a reasonable shape for the achievable resolution for embedded objects in the quasidiffuse case is also the geometric average of the achievable resolutions for slabs of thicknesses  $\delta$  and  $d - \delta$ . Mathematically, this is represented by

$$\mathcal{R}^E(\delta, d) \approx \sqrt{\mathcal{R}(\delta)\mathcal{R}(d - \delta)}. \quad (25)$$

The best achievable resolution of embedded objects in all cases can therefore be determined from the data in Fig. 6 using Eq. (25).

It is instructive to compare the foregoing results with other reported results in the literature. Since we have argued that the achievable resolution is only a weak function of the system sensitivity, comparison of the best reported results of different groups should agree with the present results. There are two common geometries em-

ployed in most reported transillumination experiments and simulations: Direct imaging of the exit surface of a slab of thickness  $d$  (denoted as surface object geometry), and imaging an embedded object at  $d/2$  in a slab of thickness  $d$  (denoted as embedded object geometry). In the present work, we have shown that the *diffusion-limited* FWHM value of the PSF is  $\mathcal{R}/d \approx 2\sqrt{\ln(2)}/5 \approx 0.33$  in the surface object geometry and one-half that value  $\mathcal{R}^E/d \approx 0.17$  for the embedded object geometry. These values can change by  $\pm 15\text{--}20\%$  depending on the system sensitivity. Reported values can also be smaller than these values if the experiments are not performed in the diffusion limit.

We will restrict the comparison only to those papers which contain enough information to deduce the FWHM values of the PSF. Mitic *et al.* [32] report (for an embedded object geometry) their best resolution as  $\mathcal{R}^E/d \approx 0.18$  for a slab 40 mm thick ( $d/l_t \sim 5$ ) and  $\mathcal{R}^E/d \approx 0.13$  for  $d/l_t \sim 2$ , both of which are consistent with the values reported here. Notice that the resolution in the case where  $d/l_t \sim 2$  is not a diffusion-limited value. Hebden [20] reports values of  $\mathcal{R}^E/d \approx 0.15$  obtained from direct imaging. (Hebden reports in the same paper a factor of 2 improvement over this value using temporal extrapolation, an advanced signal processing technique.) Hee *et al.* [18] report a best resolution of  $\mathcal{R}^E/d \sim 0.03$  using the quasi-ballistic light that followed the clearly visible ballistic peak. In a similar experiment that used chicken muscle as a phantom, Chen [33] reports PSF's as narrow as  $\mathcal{R}/d \approx 0.06$ ; however, it is difficult to discuss the meaning of this number since chicken muscle is notoriously difficult to characterize, and no measure of the transport length was reported in this paper. Andersson-Engels *et al.* [12] report the detection (at a roughly 50% contrast level) of a 5-mm sphere embedded in a 35-mm slab, implying roughly that  $\mathcal{R}^E/d \sim 0.14$ . Thus all reported best-case values of the FWHM of the PSF to our knowledge are consistent with the results contained in the present paper.

Finally, this work sets some practical limits on what resolution will be achievable in a medical imaging situation. For  $g = 0.92$ , which is fairly typical of tissue [31], we have shown that the sample thickness for which any significant improvement beyond the diffusion-limited resolution is achievable is approximately less than five transport lengths, or 60 scattering lengths. Thus, for embedded abnormalities more than five transport lengths from an exit surface, the diffusion limit should work adequately for predicting the achievable resolution at arbitrarily short integration times for imaging systems that collect one photon in  $10^{10}$  launched.

#### ACKNOWLEDGMENTS

This work was supported by the Office of Naval Research. J.A.M. and P. R.B. acknowledge support from the National Research Council. The authors acknowledge stimulating discussions with R. H. Lemberg of Naval Research Laboratory and Judith Prewitt of the PAXX Group.

#### APPENDIX A: SOLUTION OF THE TIME-DEPENDENT ISOTROPIC-SCATTERING RADIATIVE TRANSFER PROBLEM

Although solutions to the time-dependent isotropic-scattering radiative transfer problem are published [23–25], they are usually of little use for direct calculation. Here we outline an asymptotic solution to the isotropic radiative transport equation which is useful for calculation of the time-dependent point-spread-function.

We start with Eq. (21). By expanding  $P^{(n)}(\mathbf{r}, t; \hat{\Omega})$  in spherical harmonics,

$$P^{(n)}(\mathbf{r}, t; \hat{\Omega}) = \sum_{lm} P_{lm}^{(n)}(\mathbf{r}, t) Y_{lm}(\hat{\Omega}), \quad (\text{A1})$$

and substituting Eq. (A1) into Eq. (21), we obtain

$$P_{lm}^{(n+1)}(\mathbf{r}, t) = \int d\mathbf{r}' dt' K_0(\mathbf{R}, t - t') P_{00}^{(n)}(\mathbf{r}', t') Y_{lm}^*(\hat{\mathbf{R}}), \quad (\text{A2})$$

where  $P_{00}^{(n)}$  is the  $l=0, m=0$  term after  $n$  collisions, and

$$K_0(\mathbf{r}, t) = \int_{4\pi} d\hat{\Omega} K(\mathbf{r}, t; \hat{\Omega}). \quad (\text{A3})$$

We note from the form of Eq. (A2) that the angular information depends only on the last collision, as expected in a Markov process.

We neglect boundaries, so we apply the infinite-space Fourier-Laplace transform to Eq. (A2) and obtain

$$\tilde{P}_{lm}^{(n)}(\mathbf{k}, s) = H_l(\mathbf{k}, s) Y_{lm}^*(\hat{\mathbf{k}}) \tilde{P}_{00}^{(n-1)}(\mathbf{k}, s), \quad (\text{A4})$$

where

$$H_l(\mathbf{k}, s) = \frac{\mu_s}{2} \frac{(ik)^l \Gamma\left[\frac{l+1}{2}\right] \Gamma\left[\frac{l+2}{2}\right]}{\left[\mu_s + \frac{s}{c}\right] \Gamma\left[l + \frac{3}{2}\right]} \times {}_2F_1\left[\frac{l+1}{2}, \frac{l+2}{2}; l + \frac{3}{2}; -\frac{k^2}{\left[\mu_s + \frac{s}{c}\right]^2}\right], \quad (\text{A5})$$

and where  $\Gamma(x)$  is the gamma function and  ${}_2F_1(a, b; c; x)$  is a hypergeometric function. When  $l=m=0$ , Eq. (A5) reduces to

$$H_0(\mathbf{k}, s) = h(k, s) = \frac{\mu_s}{2ik} \ln \left[ \frac{\left[\mu_s + \frac{s}{c}\right] + ik}{\left[\mu_s + \frac{s}{c}\right] - ik} \right]. \quad (\text{A6})$$

By using induction, and the fact that  $\tilde{P}_{00}^{(0)}(\mathbf{k}, s) = 1$ , we find that

$$\tilde{P}_{00}^{(n-1)}(\mathbf{k}, s) = [h(k, s)]^{n-1}, \quad (\text{A7})$$

so that Eq. (A4) becomes

$$\tilde{P}_{lm}^{(n)}(\mathbf{k}, s) = H_l(\mathbf{k}, s) Y_{lm}^*(\hat{\mathbf{k}}) [h(k, s)]^{n-1}. \quad (\text{A8})$$

The problem is therefore reduced to finding the inverse Fourier-Laplace transform of Eq. (A8).

We will first concentrate on the inverse spatial Fourier transform. It is necessary to invoke analytic continuation into the complex- $k$  plane in order to evaluate the inverse transform of  $\tilde{P}$ . We must be careful to work with the total probability, so the function to be continued is

$$\tilde{P}_{lm}(\mathbf{k}, s) = \frac{H_l(\mathbf{k}, s) Y_{lm}^*(\hat{\mathbf{k}})}{1 - h(k, s)}, \quad (\text{A9})$$

which is Eq. (A8) formally summed from  $n = [1, \infty)$ .

We rewrite Eq. (A9) as

$$\tilde{P}_{lm}(\mathbf{k}, s) = H_l(\mathbf{k}, s) Y_{lm}^*(\hat{\mathbf{k}}) \left[ 1 + h(k, s) + \frac{[h(k, s)]^2}{1 - h(k, s)} \right], \quad (\text{A10})$$

and treat the  $n = 1$  (ballistic) and  $n = 2$  terms as special cases.

Concentrating on the third term in Eq. (A10), which we call  $\tilde{P}'_{lm}$ , we evaluate the  $\hat{\mathbf{k}}$  part of the Fourier integral to obtain

$$\tilde{J}_0(r, s) = \frac{\mu_s^3}{16(2\pi)^2 \mu_s r} \int_{-\infty/(1+s\tau_s)}^{\infty/(1+s\tau_s)} \frac{du}{u^2} \frac{\left[ \ln \left[ \frac{1+iu}{1-iu} \right] \right]^3 [e^{i(1+s\tau_s)u\mu_s r} - e^{-i(1+s\tau_s)u\mu_s r}]}{s\tau_s + 1 - \frac{\tan^{-1}(u)}{u}}. \quad (\text{A14})$$

Figure 13 shows the contour used for the positive-exponent term of Eq. (A14) (the negative exponent term makes exactly the same contribution over a similar contour closed in the lower-half- $u$  plane). There may be simple poles in the  $u$  plane which will lead to residue terms, as well as the integrals along the branch cuts. By further substituting  $u = i + ye^{\pm i\pi/2}$  along the right and left sides of the branch cut, respectively, and by using the residue theorem, we obtain the result that

$$\begin{aligned} \tilde{I}_0(r, s) &= 2\pi i \sum_j R(j) + \frac{\mu_s^3}{16(2\pi)^2 i \mu_s r} \\ &\times \int_0^\infty \frac{dy e^{-(1+s\tau_s)(1+y)\mu_s r}}{(1+y)^2} \\ &\times [L_+(y, s) - L_-(y, s)], \quad (\text{A15}) \end{aligned}$$

where

$$L_\pm(y, s) = \frac{\left[ \ln \left[ \frac{y}{2+y} \right] \pm i\pi \right]^2}{s\tau_s + 1 + \frac{1}{2(1+y)} \left[ \ln \left[ \frac{y}{2+y} \right] \pm i\pi \right]}. \quad (\text{A16})$$

We claim that we can neglect the residue terms at short times. We justify this by noting that Eq. (A9) can be expanded for any  $\mathcal{N}$ ,

$$\tilde{P}'_{lm}(\mathbf{r}, s) = \tilde{J}_l(r, s) Y_{lm}^*(\hat{\mathbf{r}}), \quad (\text{A11})$$

where we have introduced the function

$$\tilde{J}_l(r, s) = \frac{4\pi(-i)^l}{(2\pi)^3} \int_0^\infty k^2 dk \frac{H_l(k, s) j_l(kr) [h(k, s)]^2}{1 - h(k, s)}, \quad (\text{A12})$$

and where  $j_l(x)$  is a spherical Bessel function.

By expanding the denominator of Eq. (A12), we also define functions in analogy with Eq. (A8),

$$\begin{aligned} \tilde{J}_l^{(n)}(r, s) &= \frac{4\pi(-i)^l}{(2\pi)^3} \\ &\times \int_0^\infty k^2 dk H_l(k, s) j_l(kr) [h(k, s)]^{n-1}. \quad (\text{A13}) \end{aligned}$$

We now restrict ourselves to the  $l = m = 0$  case. The  $l, m \neq 0$  cases introduce no fundamentally new mathematics, only somewhat more tedious algebra. Defining the scattering time  $\tau_s = 1/(c\mu_s)$ , we conformally map onto a variable  $u = (k/\mu_s)/(1+s\tau_s)$  which leaves an integral in the complex- $u$  plane,

$$\tilde{P}_{lm}(\mathbf{k}, s) = H_l Y_{lm}^*(\hat{\mathbf{k}}) \left[ 1 + h + h^2 + \dots + h^{\mathcal{N}} + \frac{h^{\mathcal{N}+1}}{1 - h(k, s)} \right]. \quad (\text{A17})$$

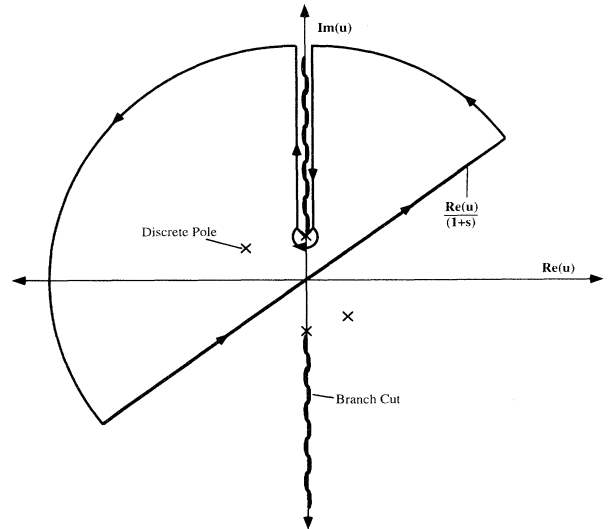


FIG. 13. Contour used to evaluate complex- $u$  integral for the positive-exponent term.

From the form of  $H_l$  it is apparent that the first  $\mathcal{N}$  terms do not contain discrete poles, and thus only the integrals along the branch cuts contribute. If the series converges in the first  $\mathcal{N}$  terms to some suitably low value, then the series is asymptotic, and should be truncated at its second-to-smallest term. In this case, the discrete residue terms can be neglected. Although we do not rigorously derive where this condition will be satisfied, with care we can tell numerically where the series is useful in its asymptotic form. We find that this series is useful until the diffusion limit is approached (as intuitively expected). We will discuss the discrete singularity contributions further below.

At short times, therefore, we may apply the inverse Laplace transform to Eq. (A3) to obtain the final result

$$\mathcal{J}_0^{(n)}(r, t) = \frac{c\mu_s^4 [\mu_s r]^{n-4} e^{-\mu_s ct}}{2^{n+1}(n-3)!} \int_0^\epsilon dy \frac{(\epsilon-y)^{n-3}}{(y+1)^{n-1}} L^{(n)}, \quad (\text{A18})$$

where

$$L^{(n)}(y) = \frac{1}{\pi^2} \left\{ \left[ \ln \left[ \frac{2+y}{y} \right] \right]^2 + \pi^2 \right\}^{n/2} \times \sin \left[ n \tan^{-1} \left[ \frac{\pi}{\ln \left[ \frac{2+y}{y} \right]} \right] \right], \quad (\text{A19})$$

and where  $\epsilon = (ct/r) - 1$ . The above procedure can be carried out for the  $l=1$  term to give

$$\begin{aligned} \mathcal{J}_1^{(n)}(r, t) &= \frac{c\mu_s^4 [\mu_s r]^{n-4} e^{-\mu_s ct}}{2^n(n-3)!} \\ &\times \int_0^\epsilon dy \frac{(\epsilon-y)^{n-3}}{(y+1)^{n-1}} \left[ 1 + \frac{\epsilon-y}{(1+y)(n-2)} \right] \\ &\times \left[ \frac{L^{(n)}}{2(1+y)} - L^{(n-1)} \right]. \quad (\text{A20}) \end{aligned}$$

$$R(j) = \frac{\mu_s^3}{16(2\pi)^2 \mu_s r} \frac{\left[ \ln \left[ \frac{1+iu_j(s)}{1-iu_j(s)} \right] \right]}{u_j^2(s) \partial_u D(u_j(s), s)} \left[ e^{i(1+s)u_j(s)\mu_s r} - e^{-i(1+s)u_j(s)\mu_s r} \right] \quad (\text{A27})$$

where we have defined

$$D(u, s) = s\tau_s + 1 - \frac{\tan^{-1}(u)}{u}. \quad (\text{A28})$$

By changing variables in the inverse Laplace transform via  $st \rightarrow z$ , we may solve for the poles given by Eq. (A26) for small  $s$  to obtain the large- $t$  behavior. This yields  $u_j(s) \simeq \pm i\sqrt{3s\tau_s}$ . Back substitution of these values leads to the form

$$\tilde{\mathcal{J}}_0(r, s) \simeq \frac{\mu_s^3}{4\pi\mu_s r} e^{-\sqrt{3s\tau_s}\mu_s r}. \quad (\text{A29})$$

When  $n=2$ , the results are

$$\mathcal{J}_0^{(2)}(r, t) = \frac{c\mu_s^4}{4\pi(\mu_s r)(c\mu_s t)} \ln \left[ \frac{\frac{ct}{r} + 1}{\frac{ct}{r} - 1} \right] e^{-\mu_s ct} \quad (\text{A21})$$

and

$$\frac{\mathcal{J}_1^{(2)}(r, t)}{\mathcal{J}_0^{(2)}(r, t)} = \frac{1}{2} \left[ \frac{ct}{r} + \frac{r}{ct} \right] - \left[ \ln \left[ \frac{\frac{ct}{r} + 1}{\frac{ct}{r} - 1} \right] \right]^{-1}. \quad (\text{A22})$$

To relate these functions to measured physical quantities of interest, we note that the angle-integrated probability can be obtained from Eqs. (A11) and (A1), which by inspection give

$$\int_{4\pi} d\hat{\Omega} P(\mathbf{r}, t; \hat{\Omega}) = \mathcal{J}_0(r, t). \quad (\text{A23})$$

The average cosine of the scattering angle between  $\hat{\mathbf{r}}$  and  $\hat{\Omega}$  after  $n$  collisions is defined as

$$C^{(n)}(r, t) = \frac{\int_{4\pi} d\hat{\Omega} (\hat{\mathbf{r}} \cdot \hat{\Omega}) P^{(n)}(r, t; \hat{\Omega})}{\int_{4\pi} d\hat{\Omega} P^{(n)}(r, t; \hat{\Omega})}. \quad (\text{A24})$$

By inspection, this is precisely

$$C^{(n)}(r, t) = \frac{\mathcal{J}_1^{(n)}(r, t)}{\mathcal{J}_0^{(n)}(r, t)}. \quad (\text{A25})$$

These are the functions used in the text.

We return now to the discrete residue terms of Eq. (A14). The poles at  $u_j(s)$  are determined from the equation

$$u_j = \tan[u_j(1+s\tau_s)]. \quad (\text{A26})$$

Unfortunately, Eq. (A26) is transcendental and does not lend itself to simple analysis; however, assuming the singularities are first order, we may formally evaluate the residues to obtain

This is precisely the Laplace transform of the infinite-space diffusion propagator, Eq. (12). Thus we see a mathematical distinction between the diffuse and quasisdiffuse photons. The discrete terms contain the diffusion limit, while the branch-cut contributions yield the quasisdiffuse photons. In other words, in the language of spectral operator analysis [25], the contribution from the discrete eigenvalues of the transport operator lead to diffusive behavior, while the contributions from the continuous eigenvalue spectrum lead to quasisdiffuse behavior.

In order to quantify at what times this approximation

will be valid, we expand  $u_j(s)$  to next higher order to obtain  $u_j(s) \simeq \pm \sqrt{3s\tau_s} [1 - (7s\tau_s/10)]$ . We will evaluate the inverse Laplace integral along the branch cut on the negative real  $z$  axis, and the integrand along this axis is

$$\int ds e^{st - \sqrt{3s\tau_s} [1 + (3s\tau_s/10)] \mu_s r} \\ = \frac{1}{t} \int dz e^{-z - i\sqrt{3(z\tau_s/t)[1 + (3z\tau_s/10t)]} \mu_s r}. \quad (\text{A30})$$

Provided the  $-z$  term in the exponent drives the integrand to zero before the second-order term  $|(3z\tau_s/t)^{3/2}/10|$  becomes significant, the diffusion approximation should be valid. This consideration implies the condition

$$\frac{t}{\tau_s} \gg \left[ \frac{3z}{10^{2/3}} \right] (\mu_s r)^{2/3}. \quad (\text{A31})$$

Assuming that the part of the integrand for  $z \geq 2$  contributes negligibly to the transform (since the integrand is

getting exponentially smaller with  $z$ ), we obtain the condition

$$\frac{t}{\tau_s} \gg \left( \frac{54}{25} \right)^{1/3} (\mu_s r)^{2/3} \sim (\mu_s r)^{2/3}. \quad (\text{A32})$$

This is the restriction on the time when the diffusion approximation is valid.

## APPENDIX B: RESOLUTION SCALING FOR EMBEDDED OBJECTS IN THE DIFFUSION LIMIT

We extend the procedure used in Ref. [17]. A more advanced method reported by Schotland, Haselgrove, and Leigh [34] yields similar results. We assume that a point source at  $\rho=0$ ,  $z=0$  emits a pulse that crosses a small volume centered at  $\rho=\rho_0$ ,  $z=\delta$ . The small volume at  $\rho_0$ ,  $\delta$  acts as a source for the detector of area  $A = \pi a^2$  in the plane  $z=d$ . We will then constrain the integration over all possible paths to some finite total time  $\tau$  to obtain a given total number of received photons as before. Mathematically, we write these operations as

$$N(\rho_0, \delta, d, \tau) = D^2 \int_0^\tau dt \int_0^t dt' \int_A d^2\rho G(\rho, z, t') G(\rho - \rho_0, d - \delta, \tau - t'), \quad (\text{B1})$$

where  $G(r, t)$  is the appropriate Green's function for the geometry chosen.

For simplicity, we will neglect the slab boundary conditions, ignore causality, and use the infinite-space Green's function. The above convolution is best evaluated in Laplace space. Using the Laplace transform of Eq. (12),

$$\tilde{G}(r, s) = \frac{e^{-\sqrt{(3sc/t_i)(r/t)}}}{4\pi D r}. \quad (\text{B2})$$

Equation (B1) can be evaluated at short times using the infinite-space propagator which gives

$$N(\rho_0, \delta, d, \tau) = \left[ \frac{3}{4\pi} \right]^{3/2} \frac{\sqrt{4\pi D} \tau a^2 \exp \left[ \frac{-[\sqrt{\rho_0^2 + \delta^2} + \sqrt{\rho_0^2 + (d - \delta)^2}]^2}{4D\tau} \right]}{\sqrt{\rho_0^2 + \delta^2} \sqrt{\rho_0^2 + (d - \delta)^2} [\sqrt{\rho_0^2 + \delta^2} + \sqrt{\rho_0^2 + (d - \delta)^2}]}, \quad (\text{B3})$$

where we have replaced the integral over detector area with  $\pi a^2$  times the value at  $\rho=0$ .

The exponent in Eq. (B3) primarily determines the shape of the PSF. To find the value of  $\rho_0 = \mathcal{R}_e^E(\delta, d)$  that gives the  $1/e$  half-width of the PSF relative to its value at  $\rho_0=0$ , we must solve

$$\left[ \frac{d}{\mathcal{R}_e^E(d)} \right]^2 \left\{ \left[ \left[ \frac{\mathcal{R}_e^E(\delta, d)}{d} \right]^2 + \left[ \frac{\delta}{d} \right]^2 \right]^{1/2} + \left[ \left[ \frac{\mathcal{R}_e^E(\delta, d)}{d} \right]^2 + \left[ 1 - \frac{\delta}{d} \right]^2 \right]^{1/2} \right\}^2 - 1 = 1 \quad (\text{B4})$$

where we have defined  $\mathcal{R}_e(d) = \sqrt{4Dt}$ . Equation (B4) can be solved to give

$$\mathcal{R}_e^E(\delta, d) \simeq \mathcal{R}_e(d) \frac{\sqrt{\delta(d - \delta)}}{d}. \quad (\text{B5})$$

It is interesting to note that a similar form for embedded resolution is obtained [35] in the time-independent case when a strong absorption is present. This is fully expected since the time gate effectively acts as an absorptive loss by cutting off the longer path lengths.

To calculate  $\mathcal{R}_e^E(d)$  we define  $\mathcal{R}_e^E(d) = d/x_0$ , and substitute this into Eq. (B3) when  $\rho_0=0$ . The result is that  $x_0$  is determined by the solution to a transcendental equation

$$N \simeq \sqrt{\pi} \left[ \frac{3}{4\pi} \right]^{3/2} \left[ \frac{a}{\delta} \right] \left[ \frac{a}{d - \delta} \right] \frac{e^{-x_0^2}}{x_0}, \quad (\text{B6})$$

which gives  $x_0 \sim 5$  as in the slab-geometry case.

- [1] P. J. Heckman, Jr. and R. T. Hodgson, *IEEE J. Quantum Electron.* **QE-3**, 445 (1967).
- [2] D. Arnush, *J. Opt. Soc. Am.* **62**, 1109 (1972).
- [3] L. B. Stotts, *J. Opt. Soc. Am.* **67**, 815 (1977).
- [4] E. P. Zege, I. L. Katsev, and I.D. Sherbaf, *Izv. Akad. Nauk SSSR, Fiz. Atmos. Okeana* **9**, 937 (1973) [*Izv. Acad. Sci. USSR, Atmos. Oceanic Phys.* **9**, 532 (1973)].
- [5] E. I. Zege, A. P. Ivanov, and I. L. Kasev, *Image Transfer Through a Scattering Medium* (Springer-Verlag, Berlin, 1991).
- [6] E. A. Bucher, *Appl. Opt.* **12**, 2391 (1973); E. A. Bucher and R. M. Lerner, *ibid.* **12**, 2401 (1973).
- [7] G. C. Mooradian, M. Geller, L. B. Stotts, D. A. Stephens, and R. A. Krautwald, *Appl. Opt.* **18**, 429 (1979).
- [8] B. Chance and R. R. Alfano, *Proc. SPIE.* **1888**, 1 (1993).
- [9] M. S. Patterson, B. Chance, and B. C. Wilson, *Appl. Opt.* **28**, 2331 (1989).
- [10] D. J. Pine, D. A. Weitz, J. X. Zhu, and E. Herbolzheimer, *J. Phys. (Paris)* **51**, 2101 (1990).
- [11] D. A. Benaron and D. K. Stevenson, *Science* **259**, 1463 (1993).
- [12] S. Anderson-Engels, R. Berg, O. Jarlmann, and S. Svanberg, *Opt. Lett.* **15**, 1179 (1990).
- [13] L. Wang, P. P. Ho, and R. R. Alfano, *Appl. Opt.* **32**, 5043 (1993).
- [14] P. P. Ho and R. R. Alfano, *Opt. Lett.* **19**, 740 (1994).
- [15] L. Wang, P. P. Ho, C. Liu, G. Zhang, and R. R. Alfano, *Science* **253**, 796 (1991).
- [16] R. R. Alfano, Z. Liang, L. Wang, and P. P. Ho, *Science* **264**, 1913 (1994).
- [17] A. H. Gandjbakhche, R. Nossal, and R. F. Bonner, *Med. Phys.* **21**, 185 (1994).
- [18] M. R. Hee, J. A. Izatt, E. A. Swanson, and J. G. Fujimoto, *Opt. Lett.* **18**, 1107 (1993).
- [19] E. A. Arons, D. Dilworth, M. Shih, and P. C. Sun, *Opt. Lett.* **18**, 1852 (1993).
- [20] J. C. Hebden, *Med. Phys.* **22**, 201 (1995).
- [21] M. D. Duncan, R. Mahon, L. L. Tankersley, and J. Reintjes, *Opt. Lett.* **16**, 1868 (1991).
- [22] J. A. Moon, R. Mahon, M. D. Duncan, and J. Reintjes, *Opt. Lett.* **18**, 1591 (1994).
- [23] R. L. Bowden and C. L. Williams, *J. Math. Phys.* **5**, 1527 (1964).
- [24] J. J. Duderstadt and W. R. Martin, *Transport Theory* (Wiley, New York, 1979), p. 59ff.
- [25] K. M. Case and P. F. Zweifel, *Linear Transport Theory* (Addison-Wesley, Reading, MA, 1967), p. 174ff.
- [26] A. Fetter and J. Walecka, *Theoretical Mechanics of Particles and Continua* (McGraw-Hill, New York, 1980), p. 430.
- [27] K. M. Case and P. F. Zweifel, *Linear Transport Theory* (Ref. [25]), p. 204ff.
- [28] J. A. Moon and J. Reintjes, *Opt. Lett.* **19**, 521 (1994).
- [29] M. Bashkansky, C. L. Adler, and J. Reintjes, *Opt. Lett.* **19**, 350 (1994).
- [30] A. H. Gandjbakhche, R. Nossal, and R. F. Bonner, *Appl. Opt.* **32**, 504 (1993).
- [31] V. G. Peters, D. R. Wyman, M. S. Patterson, and G. L. Frank, *Med. Phys. Biol.* **35**, 1317 (1990).
- [32] G. Mitic, J. Kolzer, J. Otto, E. Plies, G. Solkner, and W. Zinth, *Appl. Opt.* **33**, 6699 (1994).
- [33] Y. Chen, *Appl. Opt.* **33**, 2544 (1994).
- [34] J. C. Schotland, J. C. Haselgrove, and J. S. Leigh, *Appl. Opt.* **32**, 448 (1993).
- [35] S. Geng, F. Zeng, and B. Chance, in *Perturbation Theory of Photon Migration in the Presence of a Single Defect, OSA Proceedings on Advances in Optical Imaging and Photon Migration*, edited by R. R. Alfano (Optical Society of America, Washington, DC, 1994), Vol. 21, p. 217.

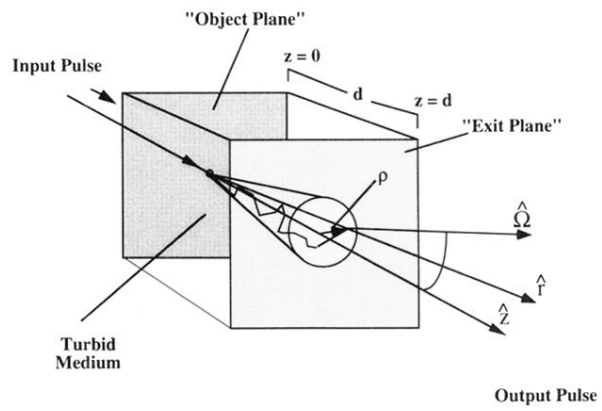


FIG. 1. Configuration used in transillumination imaging with scattered light.

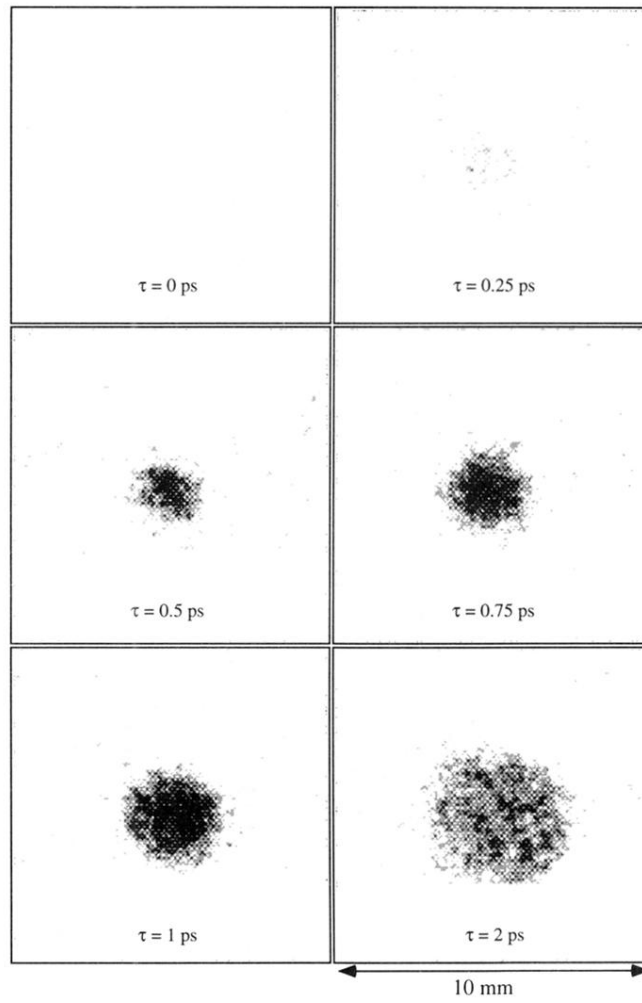


FIG. 10. Series of images taken through 25 scattering lengths of polystyrene spheres suspended in water ( $g=0.92$ ) when the ballistic component is not present. The physical sample thickness is 1 cm.

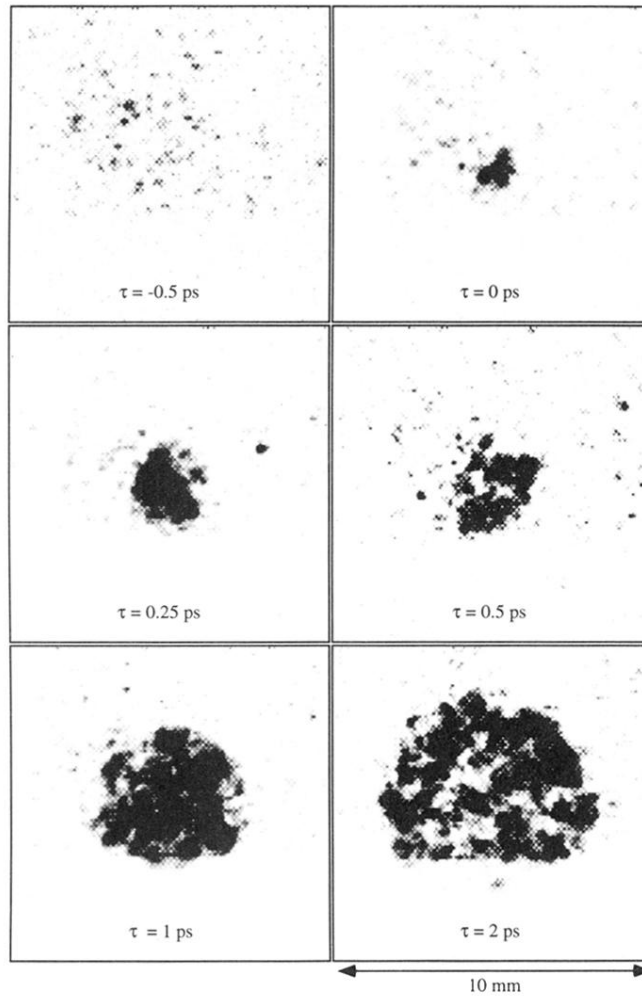


FIG. 12. Series of images taken through  $\mu_s d = 69$  scattering lengths of  $g = 0.995$  glass spheres in glycerol. The speckle size is much larger than expected for an incoherent of the same size, showing that the scattering is correlated. The physical sample thickness is 1 cm.